



European volcanological supersite in Iceland: a monitoring system and network for the future

Report

D8.2 - Case study analysis using satellite-borne microwave retrieval algorithms and sensor synergy

Work Package:	<i>Distribution and description of eruptive products</i>		
Work Package number:	8		
Deliverable:	<i>Case study analysis using satellite-borne microwave retrieval algorithms and sensor synergy</i>		
Deliverable number:	8.2		
Type of Activity:	RTD		
Responsible activity leader:	Frank S. Marzano		
Responsible participant:	Centre of Excellence CETEMPS – University of L’Aquila		
Authors:	Frank S. Marzano (CETEMPS), Mario Montopoli (CETEMPS), Domenico Cimini (CETEMPS)		

Type of Deliverable:	Report	<input checked="" type="checkbox"/>	Demonstrator	<input type="checkbox"/>
	Prototype	<input type="checkbox"/>	Other	<input type="checkbox"/>
Dissemination level:	Public	<input checked="" type="checkbox"/>	Restricted Designated Group	<input type="checkbox"/>
	Prog. Participants (FP7)	<input type="checkbox"/>	Confidential (consortium)	<input type="checkbox"/>



Abstract.

Microphysical sensitivity of satellite microwave brightness temperatures to volcanic tephra of erupted plumes suggests their exploitation in synergy with satellite thermal infrared radiometer and ground-based microwave radar observations. In order to investigate this correlation, the sub-glacial Plinian explosive eruption of the Grímsvötn volcano, occurred on May 2011, is first analyzed and quantitatively interpreted by using ground-based weather radar data and the Volcanic Ash Radar Retrieval (VARR) physically-based technique. The 2011 Grímsvötn eruption has been continuously monitored by the Keflavík C-band weather radar, located at a distance of about 260 km from the volcano vent. Radar-based ash retrieval results are then compared with available imagery from the Special Sensor Microwave Imager Sounder (SSMIS) conically-scanning microwave radiometer aboard the DMSP satellite in order to show the potential contribution and limitations of these microwave remote sensing products to the understanding and modeling of explosive volcanic ash eruptions. A detection algorithm, based on SSMIS channel frequencies above 150 GHz, is proposed and applied. Spaceborne microwave brightness temperatures show a correlation with ash columnar content, derived from VARR, depending on the millimeter-wave frequency and on the spatial averaging. A semi-empirical algorithm to estimate tephra loading from SSMIS and from the Microwave Humidity Sounder (MHS), a cross-track microwave radiometer aboard the NOAA and MetOP satellites with characteristics similar to the 5 higher frequency channels of SSMIS, is discussed and applied to available data of the Grímsvötn eruption on May 2011. A model-based analysis is discussed to investigate the role of the atmospheric state on the microwave radiometric signatures. The major conclusion of this work is the experimental confirm of the appealing potential of spaceborne microwave radiometer observations to monitor the erupted plume due to its sensitivity to the volcanic tephra in the proximity of the eruption vent (where satellite-based infrared measurements saturate their signature due to the presence of large particles and significant optical thickness). On the other hand, the major limitation of current spaceborne microwave radiometers for tephra loading detection and retrieval remains its poor spatial resolution (of the order of 15x15 km at frequency larger than 85 GHz) which limit the sensitivity to ash loadings larger than at 0.1 kg/m² and coarse to large ash particles (larger than 50 microns of diameter). Synergetic multi-sensor approaches may be an interesting perspective to better exploit the potential of spaceborne microwave radiometers for plume monitoring.

Outline

1. INTRODUCTION	2
2. MULTISENSOR OBSERVATION OF VOLCANIC PLUME	3
2.1 Tephra mapping from C-band radar data	3
2.2 Spaceborne microwave radiometric signatures.....	5
2.3 Ash plume detection from spaceborne microwave radiometric measurements.....	7
3. MICROWAVE RADIOMETRIC RETRIEVAL OF ASH LOADING	9
3.1 Tephra columnar content estimate from spaceborne microwave radiometric data.....	9
3.2 Model-based sensitivity analysis of tephra retrievals	12
4. CONCLUSION	14
REFERENCES.....	15

1. INTRODUCTION

The prompt detection of explosive volcanic eruptions and accurate determination of eruption-column altitude and ash-cloud movement are critical factors in the mitigation of volcanic risks to aviation and in the forecasting of ash fall on nearby communities (Prata and Barton, 1991; Sparks et al., 1997). On the one hand, civil prevention and protection procedures can be effectively activated if early warning is emitted in due time when quantitative information about volcanic explosions are available to the decision makers (Tupper et al., 2007). On the other hand, volcanic ash transport and fallout models are used to mitigate the hazards posed by volcanic ash, but their practical use requires, in addition to adequate computing power, estimates of eruption source parameters (Sparks, 1986; Bonadonna and Houghton, 2005; Stohl et al., 2011). These parameters, which can be typically estimated in near real-time by visual inspection (if possible) and seismic measurements, include the eruption onset time, volcanic cloud altitude and explosive activity duration (Vogfjörð et al., 2005).

Other volcanic source factors, such as the vertical distribution of ash mass and ash particle size distribution, are not easily retrievable during the eruption phase due to difficulty of direct probing and intrinsic microphysical variability (Stewart et al., 2008). Satellite remote sensing techniques can be exploited for this purpose, using thermal infrared channels available on both Low Earth Orbit (LEO) and Geostationary Earth Orbit (GEO) satellites (Wen and Rose, 1994; Gangale et al., 2010). Due to the strong optical extinction of ash cloud top layers, optical and infrared spaceborne imagery can provide a good estimate of the fine ash cloud coverage, but a less accurate estimate of its concentration and columnar content affected by water vapor and the possible presence of ice particles and aggregates (e.g., Yu et al., 2002; Grainger et al., 2013).

More recently, by exploiting the well established techniques used for physically-based radar remote sensing of rainfall, the weather radar backscattered power has been used to derive quantitative estimates of volcanic eruptive mass, ash fall out and ash size category (Marzano et al., 2006b, 2010a, 2011). The inversion of microwave radar measurements of ash clouds, called Volcanic Ash Radar Retrieval (VARR) algorithm, is founded on a physically-based forward reflectivity model coupled with a Bayesian classification and regression retrieval of ash concentration and fallout intensity (Marzano et al., 2006a). The VARR approach has been also combined with the outputs of a microphysical mesoscale volcanic eruption model and extended to deal with non-spherical ash particles using X-band dual-polarized radars (Marzano et al., 2010b; Marzano et al., 2012a).

The major volcanic parameters, derived from the time series of radar data three-dimensional (3D) volumes, are basically the distribution of ash concentration and fallout with a spatial resolution depending on the radar schedule (e.g., between few hundreds of meters to few kilometers) and a time resolution of few minutes. From this geophysical retrieval within an area of a hundred of square kilometers around the volcano vent, both total ash volume and mass due to the eruption event together with near-surface ash load, maximum height of volcanic cloud and eruption discharge rate can be obtained (Marzano et al., 2011). It should be pointed out that, depending on the distance and the radar sensitivity, for the 2011 Grímsvötn case study VARR ash products basically include coarse ash and lapilli fallout, whereas fine ash particles are generally not detected. However, the latter represents only a small fraction of the total erupted volume, even though the fine ash plume can be dispersed very far from the vent (Wen and Rose, 1994).

The present deliverable is devoted to the description and discussion of new results of VARR methodology, applied to the recent sub-glacial Plinian explosive eruptions of Icelandic Grímsvötn volcano, whose maximum activities occurred in May 2011 (Showstack, 2011). The 2011 Grímsvötn eruption has been monitored and measured by the Keflavík C-band weather radar at a distance of about 260 km from the volcano vent in the same way to the eruption of 2004. The prevailing southerly winds stretched the plume toward the Arctic pole, thus preventing the ash plume to move towards continental Europe and threatening the airline traffic. This fortunate circumstance is probably the reason for the reduced interest of the international community for the 2011 Grímsvötn eruption with respect to 2010 Eyjafjöll one (Stohl et al., 2011).

The sub-Plinian ash cloud in Eyjafjöll was persistent and fine-grained, while the ash in Grímsvötn was coarser and not as dangerous as for Eyjafjöll since it fell to the ground faster. Radar-based ash retrieval results for the Grímsvötn eruption cannot be compared with ground measurements

due to the lack, so far, of ash loading sampling and drills, but they have been qualitatively and quantitatively compared with available satellite microwave radiometric imagery. The latter represents an appealing technique to extract an estimate of ash cloud concentration, even though its operational use is limited by the low temporal repetition typical of the LEO platforms (Delene et al., 1996).

This Report D8.2 is structured as follows. In Section 2 the 2011 Grímsvötn eruption is described together with available radar imagery and products in terms of space-time volcanic cloud products. This section is aimed at showing complementary remote sensing data, based on spaceborne microwave radiometer measurements, in order to corroborate radar-based estimates of tephra as ground ash-loading samples are not available yet. Section 3 is devoted to the exploitation of microwave radiometers for tephra loading retrieval and its comparison with ground-based radar products. Moreover, a refined forward model is used to investigate the sensitivity of microwave radiometric signatures to atmospheric state. Section 4 is dedicated to conclusions and future perspectives.

2. MULTISENSOR OBSERVATION OF VOLCANIC PLUME

As mentioned, the VARR algorithm, applied to radar data gathered during the Grímsvötn volcano eruption, can be exploited to derive mass concentration, maximum height of the ash cloud, total mass and volume and spatial tephra distribution. The VARR methodology is well illustrated elsewhere (Marzano et al., 2006, 2007, 2010). After illustrating C-band radar products, spaceborne radiometric signatures of the event are discussed together with the development of a detection algorithm. Finally, by using the comparison between C-band radar and Special Sensor Microwave Imager Sounder (SSMIS) data, an empirical algorithm for tephra columnar content retrieval from SSMIS imagery is presented and discussed.

2.1 Tephra mapping from C-band radar data

From the near-surface retrieved ash fall rate $R_a(\rho, \varphi, t)$, obtained by performing a vertical profile reconstruction, we can derive the spatial distribution of the radar-based deposited tephra density or loading $D_a(\rho, \varphi)$. The latter can be extracted from the time integral of $R_a(\rho, \varphi, t)$ over the available time step by assuming an average constant eruption activity in that interval (of 5 minutes). The retrieved ash mass loading $D_a(\rho, \varphi)$ is shown in **Fig. 1** in correspondence of some time steps. This figure confirms that coarse ash and lapilli are confined within a relatively small area around the volcano vent with values larger than 200 kg/m^2 .

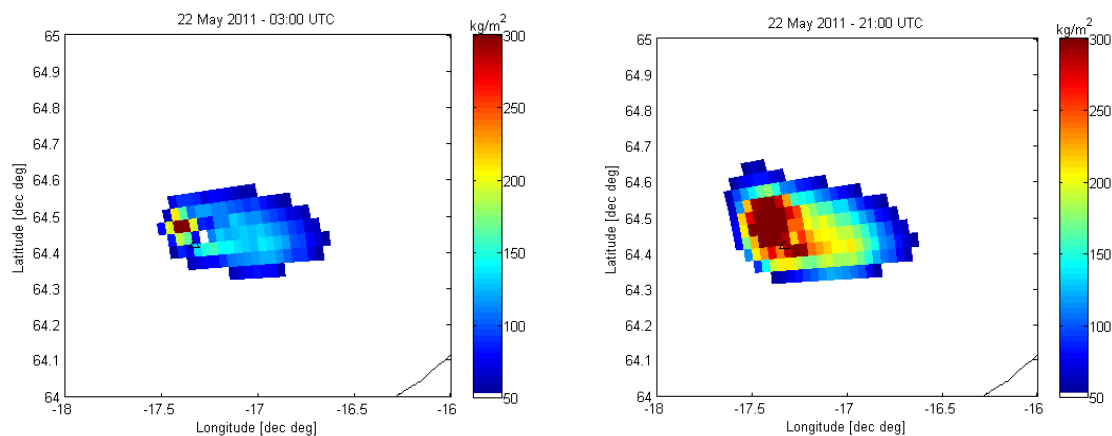


Fig. 1. Distal fallout spatial maps, retrieved by VARR, in terms of columnar ash content (kg/m^2). The distributions show 2 time steps at 03 and 21 UTC of the accumulated ash mass at the ground, computed every 3 hours from May 22, 2011 from 00:00 UTC till 21:00 UTC. The black edged triangle is centered in the exact position of the Grímsvötn volcano, whereas colorbars are chosen in order to match the different dynamic range of the distributions.

The total erupted ash mass M_{aT} can be evaluated through the spatial integration of the instantaneous deposited tephra $D_a(\rho, \varphi)$, derived from VARR. The total volume V_{aT} of the eruption event is then obtained from the estimated mass M_{aT} . **Table 1** shows the intercomparison results in terms of overall mass M_{aT} and volume V_{aT} as retrieved by means of VARR methodology. Note that, in order to provide an intrinsic variability of VARR estimates, estimations have been carried out considering: i) 2 different ash fallout models derived from Harris and Rose (1983) and from Wilson (1972); ii) an uncertainty of the estimated ash fall rate R_a equal to minus or plus the estimation standard deviation, derived from estimation error analysis due to the best fit of the regression curve. Note that values in Tab. 1 of V_{aT} are in the order of magnitude of $3.5 \cdot 10^8 \text{ m}^3$ and they well agree with the VEI-4 classification given to the 2011 Grímsvötn eruption. Indeed, values of eruption volume in the range $[10^8, 10^9] \text{ m}^3$ are expected for a VEI-4 eruption.

Table 1. Total mass and total volume values for the May 21-28, 2011 eruption period, obtained from radar-derived ashfall rate R_a by selecting fall velocity values a_v and b_v , derived from the Harris and Rose (1983) ash fallout (HAF) data and the Wilson (1972) ash fallout (WAF) data. Sensitivity of total mass volume to the standard deviation of estimated ashfall rate, indicated by $\sigma(R_a)$, is also shown.

Source	Fallout model	Total mass [kg]	Total volume [m ³]
VARR using $R_a - \sigma(R_a)$	HAF	$4.5968 \cdot 10^{11}$	$3.8307 \cdot 10^8$
VARR using R_a	HAF	$4.6535 \cdot 10^{11}$	$3.8779 \cdot 10^8$
VARR using $R_a + \sigma(R_a)$	HAF	$4.6549 \cdot 10^{11}$	$3.8791 \cdot 10^8$
VARR using $R_a - \sigma(R_a)$	WAF	$4.2487 \cdot 10^{11}$	$3.5406 \cdot 10^8$
VARR using R_a	WAF	$4.2384 \cdot 10^{11}$	$3.5320 \cdot 10^8$
VARR using $R_a + \sigma(R_a)$	WAF	$4.2511 \cdot 10^{11}$	$3.5426 \cdot 10^8$

For volcanological purposes, it would be of much interest to quantitatively compare the ground ash estimates between different eruptions, possibly using the same sensor and retrieval technique. To this aim, **Fig. 2** shows the comparison between the total distal fallout spatial maps, retrieved by VARR, in terms of columnar ash content (kg/m^2) between the Grímsvötn volcano eruption in 2011 (left panel, from May 21, 2011 at 23:55 UTC till May 28, 2011 at 23:55 UTC) and in 2004 (right panel, from 21:20 UTC on Nov. 1, 2004 till 09:55 UTC on Nov. 3, 2004). Note that the total distal fallout in 2011 has peaks up to ten times larger than in 2004 even though the latter had a duration five times longer.

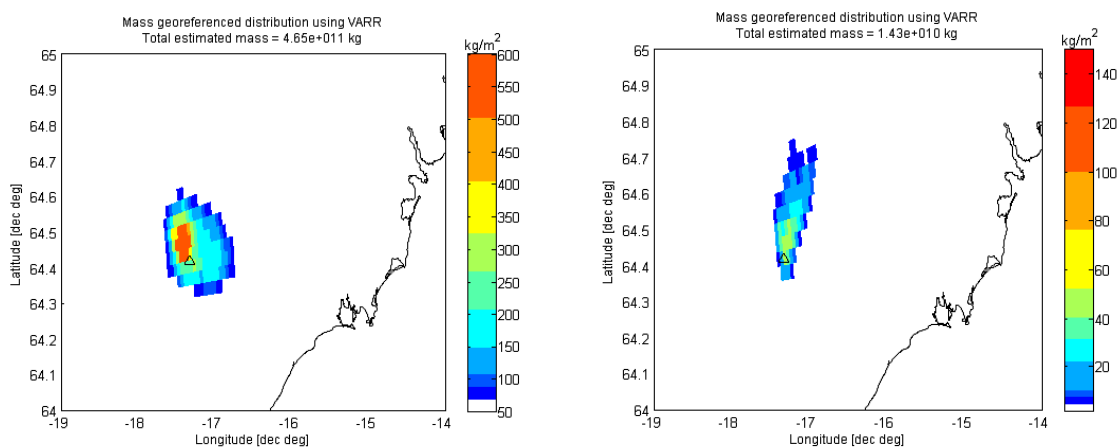


Fig. 2. Comparison between the total distal fallout spatial maps, retrieved by VARR, in terms of columnar ash content (kg/m^2) between the Grímsvötn volcano eruption in 2011 (left panel, from May 21, 2011 at 23:55 UTC till May 28, 2011 at 23:55 UTC) and the Grímsvötn volcano eruption in 2004 (right panel, from 21:20 UTC on Nov. 1, 2004 till 09:55 UTC on Nov. 3, 2004).

Radar-derived retrievals cannot be compared with ground ash samples and drills due to unavailability of the latter till now. A comparison between radar-based estimates and corresponding ground ash sampling has been carried out for the previous 2004 Grímsvötn volcano eruption (Vogfjörð et al., 2005; Marzano et al., 2010). The comparisons suggest that, at least for this subglacial eruption, the surface tephra mass, estimated by using the VARR inversion approach, is in a fairly good agreement with in situ measurements in terms of spatial extension, distribution, and amount. As

a matter of fact, most volcanoes are very often out of range of operational radar systems for meteorological monitoring.

Satellite-based ultraviolet sensors are used to study volcanic gas clouds and infrared sensors are used to track and characterize volcanic ash clouds in the atmosphere for up to several days after an eruption. However, near the volcanic vent, most of volcanic ash clouds are opaque in the ultraviolet to infrared region and appear as thick as meteorological clouds. Thus, near the volcanic vent, visible-infrared (VIS-IR) sensors aboard LEO and GEO satellites are of limited use in determining the particle size distribution and mass (Wen and Rose, 1994; Gangale et al., 2010).

2.2 Spaceborne microwave radiometric signatures

In this respect, passive observations from Microwave (MW) radiometers on LEO satellites can offer useful complementary information due to the relatively low microwave extinction and high thermal emission of ash clouds (Delene et al., 1996). This means that microwave Brightness Temperature (BT) is sensitive to the whole ash column and not only to the upper part as typical for VIS-IR radiometers both on LEO and GEO satellites. The major disadvantage of LEO microwave radiometers is the relatively poor spatial resolution which is of the order of few kilometers around 180 GHz up to tens of kilometers around 30 GHz (Yan and Weng, 2008). It is worth mentioning that the remote sensing principle of MW radiometers is completely different from that of MW radars, the latter being an active sensor based on backscattering response whereas the first a passive sensor detecting the thermal emission and multiple scattering (e.g., Wilheit et al., 1994; Marzano et al., 1999).

Table 2: Radiometric characteristics of the spaceborne SSMIS instrument (H: horizontal; V: vertical; RC: right circular)

Frequency (GHz)	Polarization (V, H, RC)	Along-track resolution (km)	Cross-track resolution (km)	Spatial sampling (km x km)	Instrument noise (K)
19.35	H, V	73	47	45 x 74	0.35
22.235	V	73	47	45 x 74	0.45
37.0	H, V	41	31	28 x 45	0.22
50.3	H	17.6	27.3	37.5 x 37.5	0.34
52.8	H	17.6	27.3	37.5 x 37.5	0.32
53.596	H	17.6	27.3	37.5 x 37.5	0.33
54.4	H	17.6	27.3	37.5 x 37.5	0.33
55.5	H	17.6	27.3	37.5 x 37.5	0.34
57.29	RC	17.6	27.3	37.5 x 37.5	0.41
59.4	RC	17.6	27.3	37.5 x 37.5	0.40
63.283248 ± 0.285271	RC	17.6	27.3	75 x 75	2.7
60.792668 ± 0.357892	RC	17.6	27.3	75 x 75	2.7
60.792668 ± 0.357892 ± 0.002	RC	17.6	27.3	75 x 75	1.9
60.792668 ± 0.357892 ± 0.005	RC	17.6	27.3	75 x 75	1.3
60.792668 ± 0.357892 ± 0.016	RC	17.6	27.3	75 x 75	0.8
60.792668 ± 0.357892 ± 0.050	RC	17.6	27.3	75 x 75	0.9
91.665	H, V	14	13	13 x 16	0.19
150	H	14	13	13 x 16	0.53
183.311 ± 1	H	14	13	13 x 16	0.38
183.311 ± 3	H	14	13	13 x 16	0.39
183.311 ± 6.6	H	14	13	13 x 16	0.56

In order to examine the sensitivity of MW BTs to the presence and intensity of ash clouds, the considered Icelandic sub-glacial Grímsvötn 2011 eruption case study is analyzed and discussed by using data from the Special Sensor Microwave Imager Sounder (SSMIS). SSMIS is a conically scanning radiometer with a swath of about 1700 km aboard the low-Earth-orbit (LEO) DMSP (United States Air Force Defense Meteorological Satellite Program) platform, first launched in 2003 (Yan and

Weng, 2008). Currently 3 satellites ensure a repetition frequency over a given area of about three overpasses per day. Specifications of SSMIS are given in **Table 2** in terms of frequency, polarization, along track and cross-track resolution, spatial sampling and instrumental noise.

Referring to horizontal and vertical polarization by H and V, respectively, **Fig. 3** shows BT images (in K) at 37V, 91V, 150H and 183±6H GHz acquired by SSMIS aboard the F-16 DMSP satellite overpassing Iceland on May 21, 2011 at 08:46 UTC during the eruption of the Grímsvötn volcano. The BT depression, which is evident in all images around the volcano vent in terms of lower values with respect to the surrounding pixels, is the signature of the plume due to ash (and, if present, ice) particle scattering of the MW radiation emitted by the land/ocean background. The MW BT of this scene is clearly frequency and surface dependent: for example, the sea is relatively “cold” at 37 GHz due to the effect of quasi-specular surface low emissivity and “warm” above 100 GHz due to the effect of atmospheric water vapor whose contribution is not anymore negligible at these frequencies (Wilheit et al., 1994). Note that the surface features can be misinterpreted: ice glaciers have a signature which can be ambiguous with respect to ash clouds, especially below 100 GHz due to the fact that both targets are relatively efficient scatters with a low emissivity (Grody and Basist, 1996). Surface BT effects are more evident below 100 GHz with a radiometric signature of the cloud-free ice cap (especially in north-west area with respect to the vent where the ash plume was not dispersed), whereas around 183 GHz the strong emission of water vapor tends to mask the surface itself, as evident in Fig. 3.

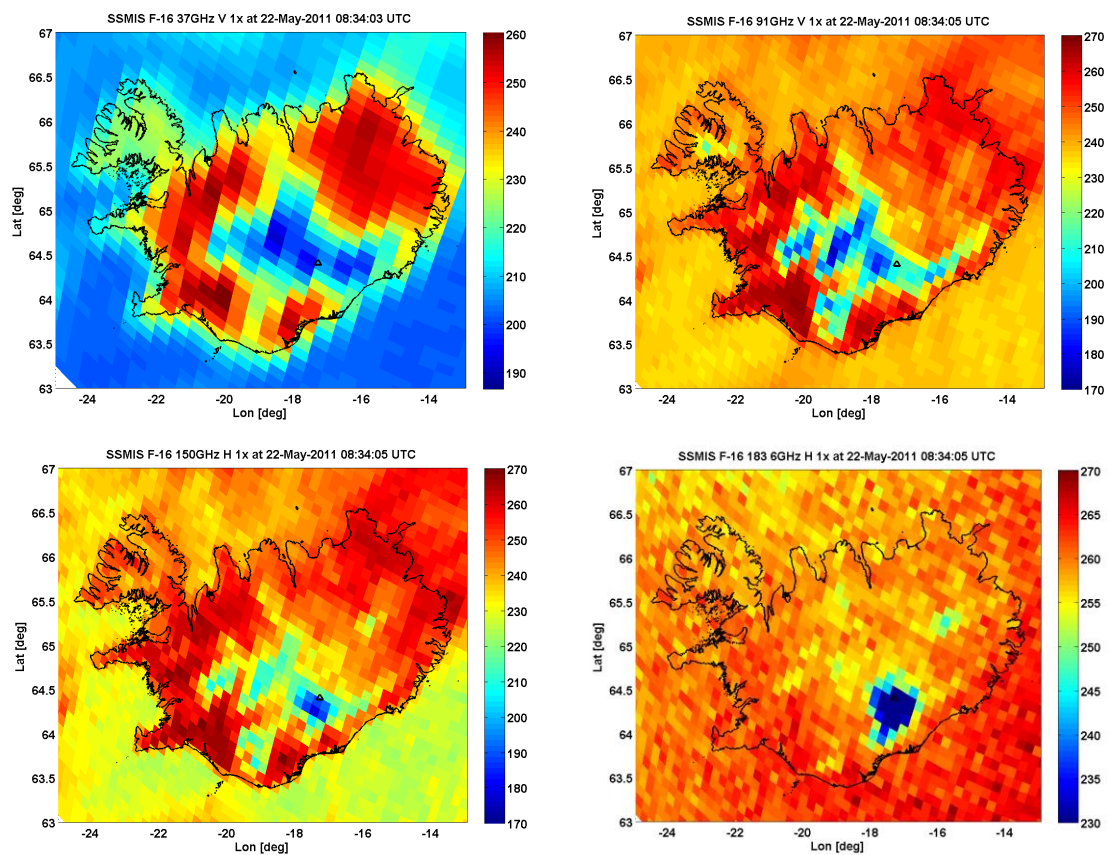


Fig. 3. Brightness temperature (BT, K) images at 37, 91, 150 and 183±6 GHz at vertical polarization, acquired by SSMIS (Special Microwave Imager Special) aboard the DMSP satellite on May 22, 2011 at 8:34 UTC during the eruption of the Grímsvötn volcano. The signature of the ash cloud is evident in all images around the volcano vent (indicated by a black triangle) as a depression of the measured BT with respect to the land BT due to tephra (and possible ice particles) scattering of land emitted radiation.

C-band radar data can be used as a ground reference for spaceborne MW BT imagery interpretation. **Fig. 4** shows two typical products derived from the C-band radar 3D data volume: the ground-projected conical map image for a fixed elevation angle, called plan-position indicator (PPI), and the vertical cross-section image, called range-height indicator (RHI). These images are shown at

08:30 and 08:35 UTC on May 22, 2011, close to the SSMIS images in Fig.3. The radar reflectivity signature is limited around the volcano vent and this suggests the ambiguous contribution of frozen surface and ash cloud affecting the BT observations below 100 GHz. MW scattering indexes have been proposed in the past to identify scattering targets, especially rainfall (Spencer et al., 1989; Delene et al., 1996). The latter exhibits a behavior which is similar to ash clouds so that some of these scattering indexes can be tested for ash cloud identification as well.

2.3 Ash plume detection from spaceborne microwave radiometric measurements

Using the distinct features between the horizontally and vertically polarized BTs, it was noted that no-rain areas over the ocean can be identified under high polarization difference and rainy areas with little polarization difference. The PCT (Polarization-Corrected Temperature) parameter is then defined by (Spencer et al., 1989):

$$PCT = 1.818 \cdot BT_V(91) - 0.818 \cdot BT_H(91) \tag{1}$$

where $BT_P(f)$ is the SSMIS brightness temperature for the P-polarized channel with $P=H$ or V at a frequency f equal to 91 GHz. Note that the original formula in Eq. (1) used the 85 GHz BT that was available on the precursor of SSMIS, i.e. the SSMI, and which we here assume to be similar to 91 GHz; different threshold values can be used to compensate for slight differences. The typical threshold for precipitation using 85 GHz BT is 255 K. The main advantage of the PCT method is its ability to reduce the effect of background surface emissivity, making it possible to delineate areas of rainfall over varying surface types.

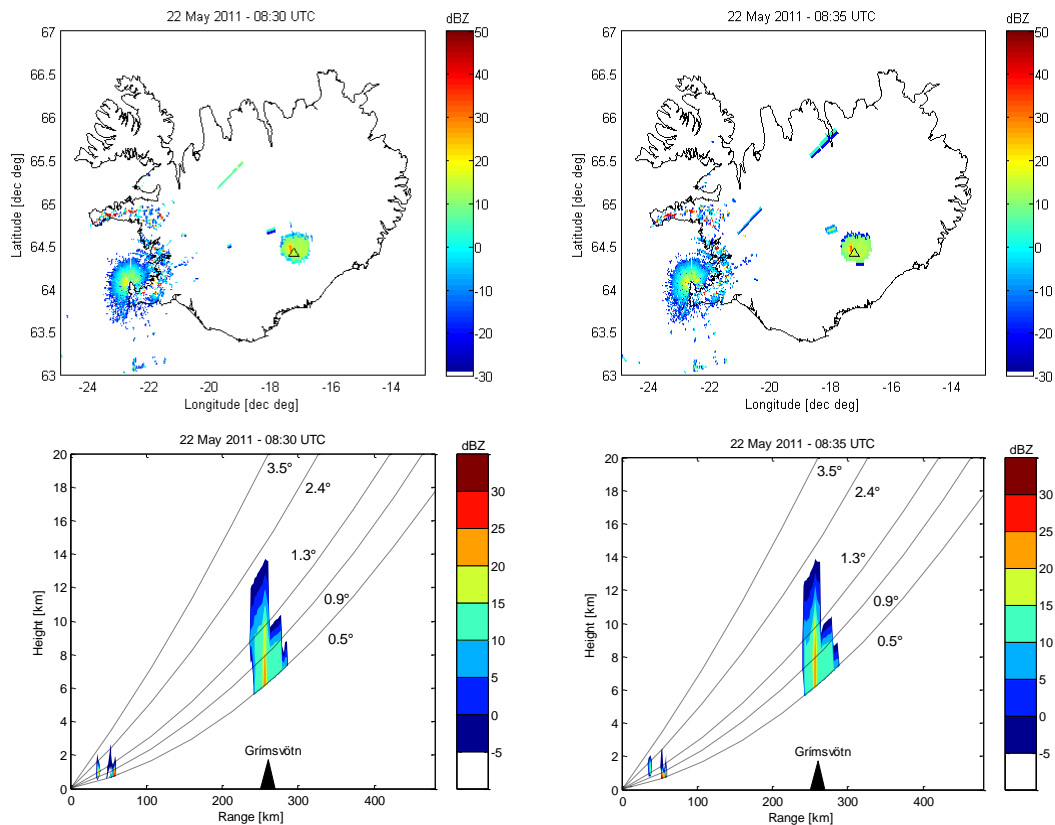


Fig. 4. Radar PPI images (top panels) and corresponding RHI images along the radar-vent line (bottom panels) at 08:30 UTC (left panels) and 8:35 UTC (right panels) on May 22, 2011.

The Scattering Index over Land (SIL) is computed by using the low-frequency channels (19 and 22 GHz) to estimate the 91 GHz BT for non-scattering conditions and then subtracting the

observed 91 GHz BT. The more radiation the area scatters, the higher SIL is. The empirical formula for SIL is (Delene et al., 1996):

$$SIL = 451.88 - 0.44 \cdot BT_v(19) - 1.775 \cdot BT_v(22) + 0.00574 \cdot BT_v(22) - BT_v(91) \quad (2)$$

where, again, as in Eq. (1), we substituted 89 GHz with 91 GHz channel frequency.

Fig. 5 shows PCT and SIL at 91 GHz at 08:34 UTC on May 22, 2011 (both derived from imagery shown in Fig. 3). In this case threshold values for PCT and SIL have been set to 250 (maximum threshold) and 10 K (minimum threshold), respectively. In Fig. 5 it is also superimposed the snow cover mask as retrieved from the same SSMI observations with an empirical threshold algorithm (Grody and Basist, 1996), fairly consistent with the monthly snow cover. The Grody-Basist snowcover detection algorithm is a decision tree based on the use of frequencies up to 90 GHz (it was developed before the launch of SSMIS) and empirically calibrated over a global scale. Since snowcover scatters high-frequency radiation, this signature provides the first step in the decision tree. Since scattering signatures also occur for precipitation, and for deserts and frozen ground surfaces when using vertical polarization, tests to filter out these conditions are applied. However, in addition to removing snow-free regions, some snow can be removed even though missing snowcover represents a small fraction of the total amount. Therefore, the snow covered surface identified by the Grody-Basist algorithm causes ambiguity in the detection of the ash cloud with PCT and SIL, as evident in Fig. 5.

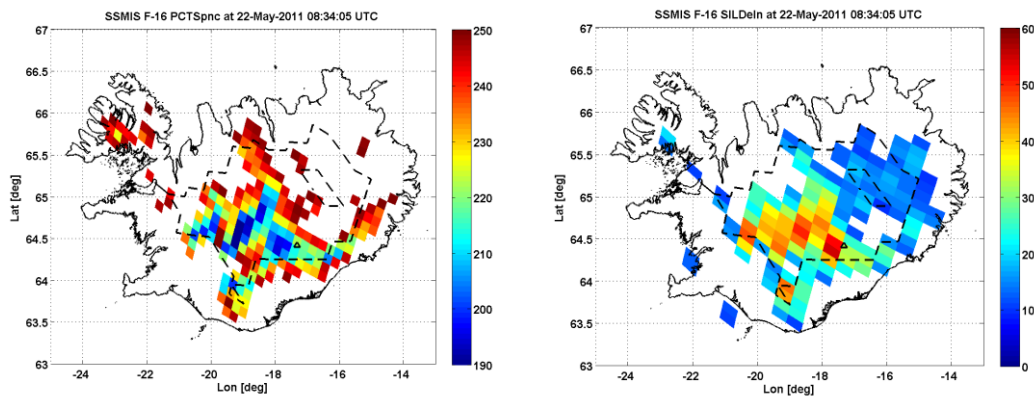


Fig. 5. (Left panel) Polarized-corrected temperature (PCT) at 91 GHz at 08:34 UTC on May 21, 2011, derived from imagery shown in Fig. 3. (Right panel) Scattering Index over land (SIL) at 91 GHz at 08:34 UTC on May 21, 2011, derived from imagery shown in Fig. 3. Dashed lines indicate the snow cover mask as retrieved from SSMIS imagery with the algorithm described in Grody and Basist (1996).

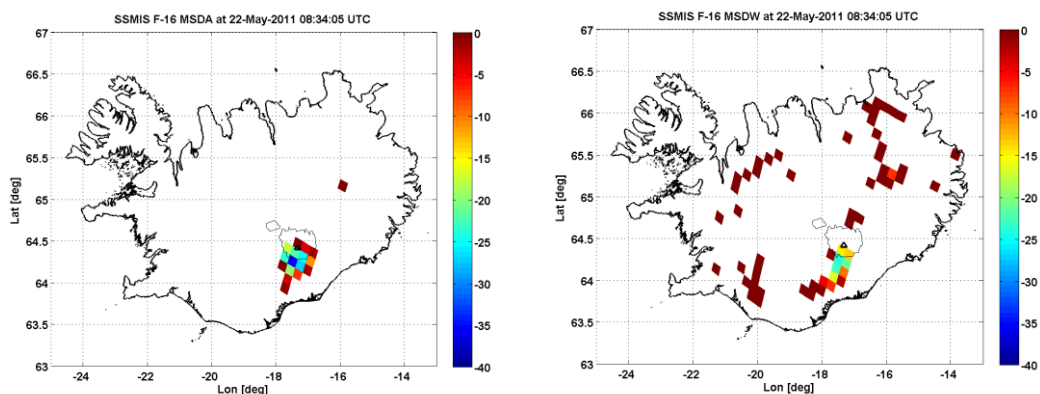


Fig. 6. Microwave Spectral Difference at Absorption bands (left panel: $MSD_A = BT_{183\pm 6} - BT_{183\pm 1}$) and at Window bands (right panel: $MSD_W = BT_{150H} - BT_{91H}$) at 08:34 UTC on May 21, 2011, derived from imagery shown in Fig. 3 (see text for details). The solid thin line indicates the area where VARR detected non-zero ash concentration around 08:35 UTC.

In order to detect ash plume within Icelandic scenario, it is most effective to exploit frequency indexes at frequencies higher than 90 GHz (which also show a relatively high and uniform spatial resolution for SSMIS: see Table 3) as the signatures at 150 and 183 GHz in Fig. 3 suggest. Two simple detection products can be derived from the SSMIS observations, hereafter named as the Absorption Microwave Spectral Difference (MSD_A) and Window Microwave Spectral Difference (MSD_W) and defined as follows:

$$\begin{cases} MSD_A = BT_H(183 \pm 6) - BT_H(183 \pm 1) \\ MSD_W = BT_H(150) - BT_H(91) \end{cases} \quad (3)$$

Fig. 6 shows these two indexes, obtained from the SSMIS observations at 08:46 UTC on May 21, 2011 in Fig. 6, assuming a minimum threshold of 0 K for both so that only positive values of MSD_A and MSD_W are considered. Note that the area where VARR detected non-zero ash concentration at 08:35 UTC (Fig. 4) is also indicated in Fig. 6. By comparing the ash detection results obtained in Fig. 6 with those of Fig. 5 it is apparent that MSDs (based on frequencies higher than 100 GHz) seem to better detect the ash plume dispersion with respect to both PCT and SIL, due to the effective mitigation of ambiguous snow surface signatures. The misplacement between the radar-based signature in Fig. 4 and SSMIS detected area in Fig. 6 may depend not only on georeferencing errors (SSMIS image may be affected by an antenna mispointing of about 1 pixel which means about 20 km), but also by a different microphysical sensitivity. Indeed, BTs at frequencies above 90 GHz (wavelengths smaller than 3 mm) are mostly sensitive to fine ash particles of about 10-100 μm which are suspended and dispersed in the middle and top layers of the troposphere, whereas C-band (wavelength of 6 cm) radar reflectivity Z_{Hm} basically responds to coarse ash and lapilli particles of about 0.1-10 mm which are falling in the surroundings of the volcanic area and are less subject to wind transportation. In addition, is worth mentioning as the ash signature obtained by the MSD approach is quite consistent with the MODIS acquisition. The latter, even though acquired nearly 3 hour before the SSMI overpass, indicate the presence of ash in the south area with respect to the volcano vent.

3. MICROWAVE RADIOMETRIC RETRIEVAL OF ASH LOADING

Ground-based measurements at the surface are usually taken as reference for remote sensing retrievals due to the sedimentation processes of ash dispersal (e.g., Marzano et al., 2012). For the 2011 Grimsvotn eruption case study ground ash samples and drills were not available so that ground-based radar data have been considered as a relatively good source of comparison with spaceborne SSMIS brightness temperature measurements. Indeed, the intercomparison between ground-based MW radar and space-based remote sensing responses is more homogenous as they are both areal measurements of airborne phenomena thus substantially different from ash loadings collected at ground at a given point after the eruption phase. The potential of microwave radiometric signatures for ash retrieval is also evaluated by resorting to the SDSU-Ash model, discussed in the Report D8.2. Sensitivity to atmospheric variables is considered and simulated.

3.1 *Tephra columnar content estimate from spaceborne microwave radiometric data*

The detection of ash cloud from space-based microwave BTs and the coregistration of SSMI and radar data can provide a first attempt to quantitatively link microwave BTs with measured copolar radar reflectivity Z_{Hm} . Note that for a direct comparison of ground-based radar and satellite radiometer observations, it is necessary to spatially average and downsample the measured reflectivity to the SSMIS footprint which is about 13 x 14 km^2 (see Table 2). This means that PPI image in Fig. 4 have been further filtered to a resolution of 14 x 14 km^2 from the available resolution at 2 x 2 km^2 . The analysis of the space-based microwave radiometric signatures of a volcanic plume is shown in terms of its consistency with the coupled forward model SDSU-Ash, described in the Report D8.1.

To this aim we have co-registered SSMIS and radar data, as shown in Section 2, in order to provide a first attempt to quantitatively relate horizontally-polarized microwave BT_H with measured co-polar radar reflectivity Z_{Hm} . Subsequently, after the collocation of the radar grid points with those from SSMIS BT_H , the instantaneous values of radar-derived particle concentration, expressed in $[kg/m^3]$, have been retrieved applying the Volcanic Ash Radar Retrieval (VARR) technique (Marzano et al., 2006, 2007). The latter has been applied to each radar vertical profile and then vertical integrals have been calculated to obtain the Total Columnar Content (TCC), expressed in $[kg/m^2]$.

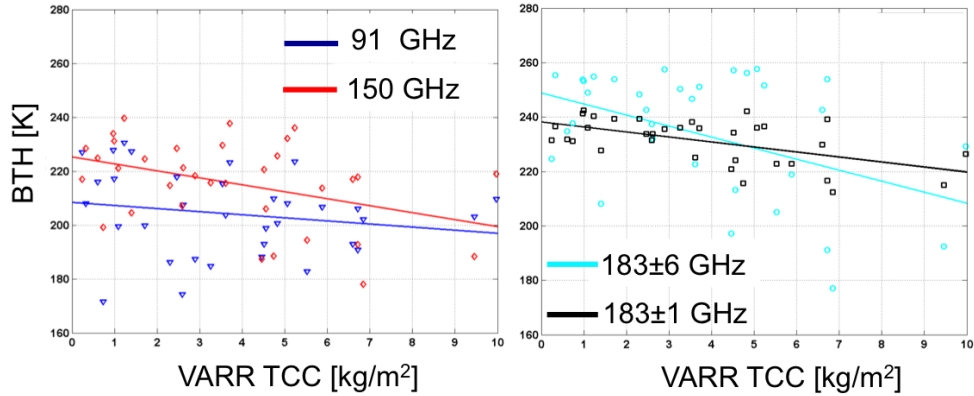


Fig. 7. Measured brightness temperature in horizontal polarization, BT_H [K] from SSMIS versus the total columnar content (TCC) $[kg/m^2]$, retrieved from ground-based C-band radar data, for SSMIS frequency channels as specified in the legend of each panel.

Table 3. BT_{Hnd} vs TCC regression Parameters from observations where BT_{Hnd} is the brightness temperatures at horizontal polarization over land

$BT_{Hnd} = a \cdot (TCC) + b, TCC [kg/m^2]; BT_{Hnd} [K]$		
Freq. [GHz]	a [m^2K/kg]	b [K]
91	-1.5	210
150	-2.5	225
183±1	-1.9	239
183±6	-3.9	249

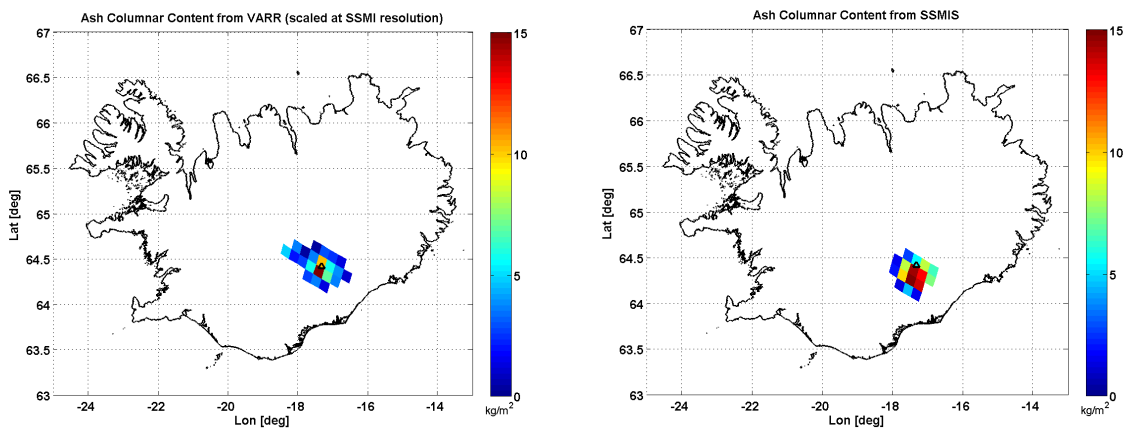


Fig. 8. (Left panel) Ash columnar content, computed from C_a profiles estimated by VARR around 08:35 UTC on May 21, 2011 and scaled onto the resolution of SSMIS. (Right panel) Estimated ash columnar content from SSMIS 183±1 GHz observations at 08:34 UTC using the linear correlation found in Fig. 7.

The result of this quantitative intercomparison is shown in **Fig. 7**. There is an evident correlation between radar-derived TCC and satellite SSMIS BT_{HS} (above 90 GHz). The correlation coefficients of BT_H at 91 and 150 GHz (left panel), 183±6 and 183±1 GHz (right panel) with TCC are, respectively, -0.37, -0.52, -0.48 and -0.63. It must be noted that the relatively high correlation between TCC and

absorbed channels around 183 GHz is due to high clear-air opacity and surface insensitivity. **Table 3** lists the regression coefficients of the empirical linear model in Fig. 7. This result potentially offers the opportunity to estimate the columnar integral of ash from BT_H once the ash detection is accomplished.

By exploiting the latter result, **Fig. 8** shows the ACC, computed from C_a profiles estimated by VARR around 08:35 UTC, i.e. the SSMI overpass on May 22, 2011, compared with that one estimated from SSMIS observations at 183 ± 1 GHz using a regressive estimator based on the $BT_H(183\pm 1$ GHz) and its linear correlation with ACC. The following is a semi-empirical algorithm, based on experimental measurements and a single-frequency channel for simplicity:

$$I_a = a + bBT_H(183\pm 1) \tag{4}$$

where I_a is the vertically-integrated (columnar) ash content and a, b are the regression coefficients of Table 3 which are independent of the surface background, but influenced by the columnar water vapor of the scene. Note that the regression coefficients a and b can be also derived from ATHAM-SDSU-Ash modeling, as described in the Report D8.1; results in this case are comparable to what shown in Fig. 8 if the surface emissivity and atmospheric state is correctly parametrized (see next section 3.2). Results of Fig. 8 may be physically questionable if we refer to the different microphysical sensitivity between BTs and Zs, as discussed before. It should be noted, however, that the radar sensitivity is significantly increased by performing a spatial average to SSMIS footprint so that the ash signature detected by the two instruments tends to be more physically consistent.

Table 4: Radiometric characteristics of the MHS (H: horizontal; V: vertical; RC: right circular)

Frequency (GHz)	Polarization (V, H, RC)	Along-track resolution (km)	Cross-track resolution (km)	Spatial sampling (km x km)	Instrument noise (K)
89.0	V	16 (nadir)	16 (nadir)	16 x 16	0.22
157	V	16 (nadir)	16 (nadir)	16 x 16	0.34
183.311 ± 1	H	16 (nadir)	16 (nadir)	16 x 16	0.51
183.311 ± 3	H	16 (nadir)	16 (nadir)	16 x 16	0.40
190.311	V	16 (nadir)	16 (nadir)	16 x 16	0.46

Using the same regression scheme described above, TCC estimates have been obtained from BT observed by the Microwave Humidity Sounder (MHS), a cross-track microwave radiometer with 5 channels with similar characteristics to the 5 higher frequency channels of SSMIS (see **Table 4**). MHS sensors are currently flying onboard of NOAA satellites as well as the European MetOp-A and -B satellites, and thus extend noticeably the number of daily overpasses above any given region. Two examples are reported in **Fig. 9**, where the TCC images estimated at 00:09 and 03:54 UTC of 22 May 2011 are shown.

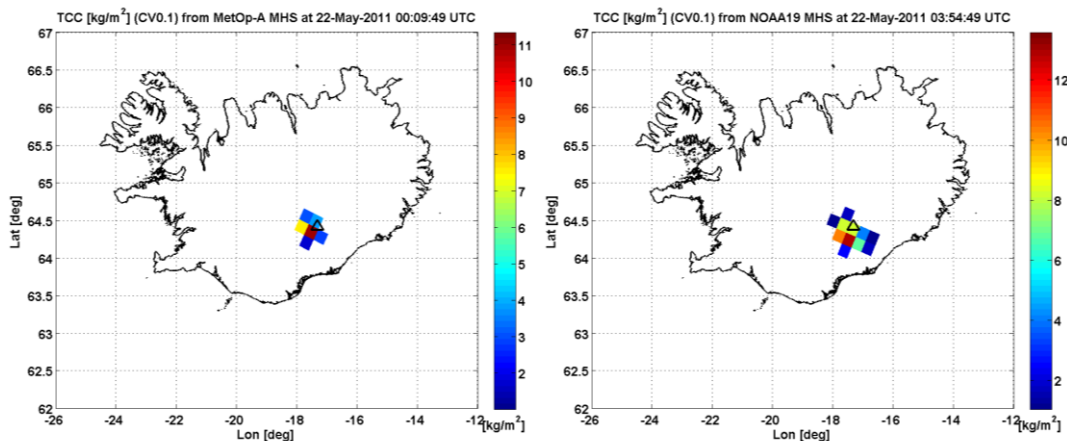


Fig. 9. Estimated total columnar content from the MHS 183 ± 6 GHz observations at 00:09 (left) and 03:54 (right) UTC using the linear correlation found in Fig. 7 and reported in Table 3.

3.2 Model-based sensitivity analysis of tephra retrievals

The considered radiometric instrument for the numerical simulations is the SSMIS, leading to a straightforward comparison with the observations previously discussed. Note that our goal here is not to reproduce the observed signature of the SSMI scene using SDSU-Ash (as it would require specific knowledge of several geophysical and atmospheric parameters), but the proper correlation and dynamic range of the SSMI BT channels. The agreement between SDSU-Ash simulations and SSMIS observations has been found quite good when performing a sensitivity analysis with respect to the surface emissivity, as discussed in the Report D8.1. A terrain emissivity between 0.7 and 0.8 explains the behavior of BT_{Hnd} from most of the considered channels. The only exception is for the channel at 183 ± 1 GHz where a strong bias is noted. Note that a variation of terrain emissivity in the range [0.7, 0.8] is consistent with either ice covered or poorly vegetated terrain, as expected in Iceland during spring.

To explain the behavior of BT_{Hnd} as a function of TCC at 183 ± 1 GHz, we have varied the water vapor and the ice content in our synthetic scenario with respect to the control configuration so far analyzed. Note that the TCC variability is obtained by choosing different ATHAM vertical profiles within the simulation domain thus foreseeing different possible ash loading scenarios. The results are shown in **Fig. 10** and **Fig. 11** in the form of linear regression curves. Grey crosses in each plot of both figures continue to give a reference in terms of SSMIS observation results. A strong reduction of water vapor (between 7% and 25%) would produce a fair agreement between observations and simulations at 183 ± 1 GHz at the cost of an evident disagreement at the other frequency channels. The variation of ice content, on the other hand, seems to produce a negligible effect at 183 ± 1 GHz, whereas it has a big impact at 150 GHz and 183 ± 6 GHz especially for larger values of TCC . These results seem to indicate that water vapor within the volcanic plume scene is distributed differently from the ATHAM control simulation and the latter tends to produce a too humid air scene, at least around the volcano vent.

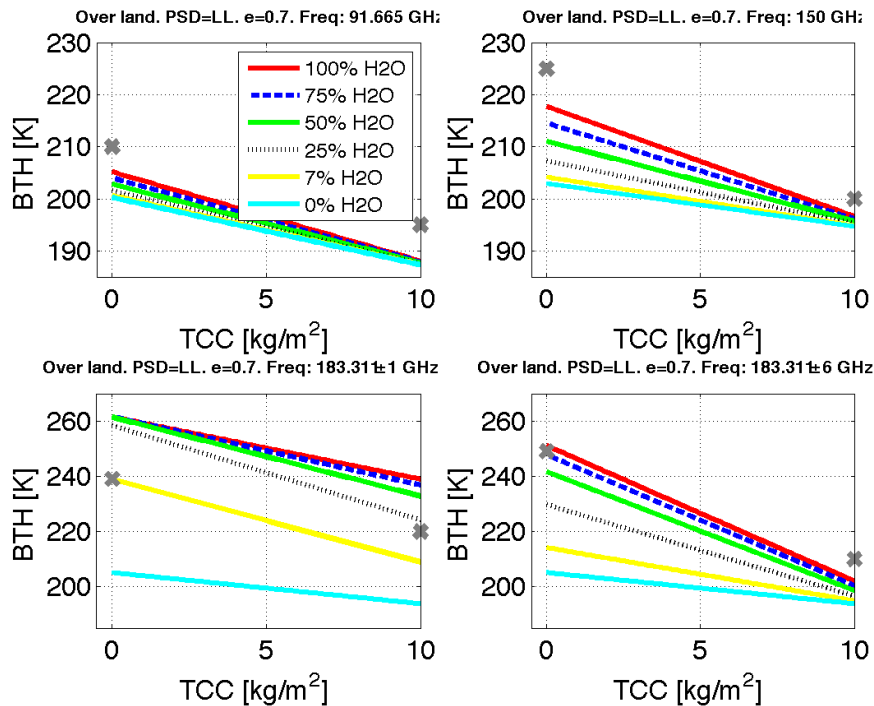


Fig. 10. Simulated brightness temperatures at horizontal polarization over land (BT_{Hnd}), for frequency channels and terrain emissivity (e) as specified in the title of each panel, vs. the synthetic Total Columnar Content (TCC) in kg/m^2 from the 2D-ATHAM (Active Tracer High-Resolution Atmospheric Model) and SDSU-Ash (Satellite Data Sensor Unit simulator for ash) simulation. Curves are obtained by varying the water vapor content as shown in the legend and considering for simplicity the linear regression curves (instead of the simulated dots).

The forward model SDSU-Ash can be used to investigate the possibility to estimate the plume height from the SSMIS-like satellite platforms. Even though this is already accomplished by ground-

based microwave radars, the support of external information, such as provided by microwave radiometers, may contribute to reduce the uncertainty that still remains on this important parameter, even though with the limitations of LEO satellite temporal sampling. **Fig. 12** shows the correlation between the ATHAM-derived plume height (h) and BT_{Hnd} at 183 ± 1 GHz, the latter derived from the SDSU-Ash simulations. The choice of other channels does not provide large variations in the results. A sixth order polynomial regression is also shown by a grey curve. The polynomial parameters are listed in **Table 5**.

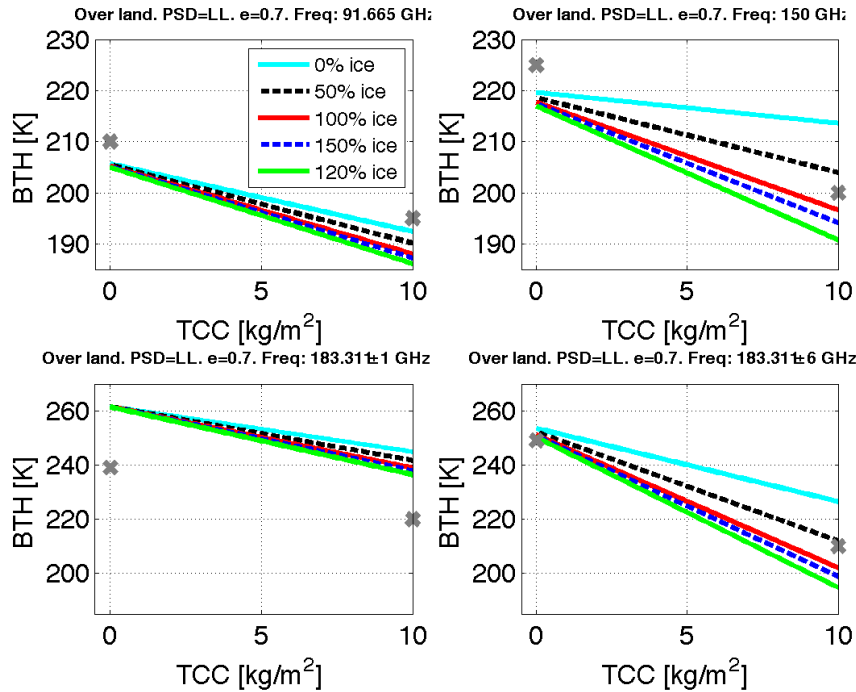


Fig. 11. As in Fig. 9, but varying the ice content as shown in the legend.

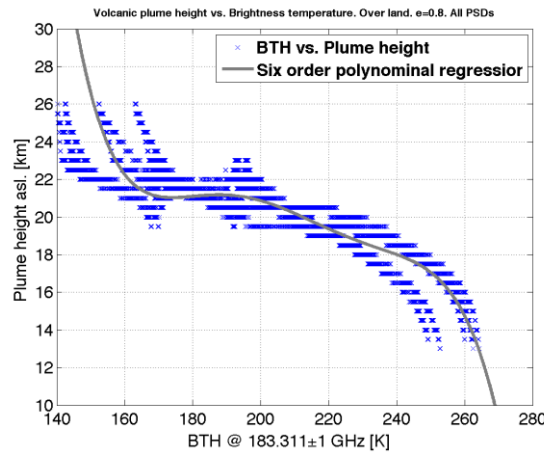


Fig. 12. Simulated correlation between the SSMIS brightness temperature and the plume height using SDSU Ash. Grey curve shows a six order polynomial regression.

At 183 ± 1 GHz, the minimum value registered for BT_{Hnd} was 212.2 K. This leads to a plume height of 20 km once the polynomial regression is applied. This value, however, is not in agreement with the 14 km height registered by the ground radar observation at the same instant. Indeed, this discrepancy may be due to the different sensitivity of the two sensors at different wavelengths, 5 cm for the C-band ground-based radar and 0.16 cm for the SSMIS channel at 183 GHz, respectively. It is well established that microwave weather radars are sensible to the presence of coarse ash and lapilli particles. The upper part of the volcanic plume (also called umbrella region) is the cloud portion

where the density of the surrounding air equals that of the rising plume, but the plume continues to rise and spreads thanks to its momentum and cross winds, respectively. The volcanic umbrella is usually characterized by fine ash particle dispersion with possible coexistence and aggregation with ice particles. Thus, smaller particles in the umbrella region could lie outside the sensitivity of the C-band radar so that this behavior can lead to an underestimation of the plume height as detected by satellite millimeter-wave radiances.

Table 5. BT_H at 183 ± 1 GHz vs. *plume height* (h : plume height in [km], BT_H : Brightness temperature in [K])

$$h = \sum_{i=0}^5 p_{6-i} BT_H^i \ln d$$

<i>Coefficients</i>			
p_1	$-1.827 \cdot 10^{-8}$	p_4	1.667
p_2	$1.920 \cdot 10^{-5}$	p_5	-171.966
p_3	-0.008	p_6	7069.5

4. CONCLUSION

The sub-glacial Plinian explosive eruption of the Grímsvötn volcano on May 2011 has been analyzed and quantitatively interpreted by using ground-based weather radar data and the volcanic ash radar retrieval (VARR) technique. Physical principles, inversion methodology and practical limitations and potentials of the VARR approach for single-polarization Doppler radars have been pointed out and discussed. The 2011 Grímsvötn eruption has been continuously monitored by the Keflavík C-band weather radar, located at a distance of about 260 km from the volcano vent. The VARR methodology has been applied to Keflavík C-band available radar time series to estimate the plume maximum height, ash particle category, ash volume, ash fallout and ash concentration every 5 minutes near the vent. Estimates of the eruption discharge rate, based on the retrieved ash plume top height, have been provided together with an evaluation of the total erupted mass and volume. Deposited ash loading has been also retrieved from radar data by empirically reconstructing the vertical profile of radar reflectivity and estimating the near-surface ash fallout. Radar-based retrieval results have not been compared with ground measurements, due to the lack of the latter, but they have been qualitatively compared with available microwave radiometric imagery in order to preliminarily show the unique contribution of these microwave remote sensing products to the understating and modeling of explosive volcanic ash eruptions.

A microwave multi-sensor analysis of the volcanic plume has been also accomplished with the aid of active and passive observations and model simulations. ATHAM volcanic plume model and SDSU sensor simulator have been coupled with some proper adaptations required to ingest volcanic plumes (instead of water clouds) into SDSU-Ash. Results support the consideration that, from a multi-frequency measurement of the satellite brightness temperature over land at horizontal polarization, it is in principle possible to estimate the total columnar content of an ash cloud near the volcano source vent. For the 2011 Grímsvötn case study this hypothesis has been proven using the available C-band ground based radar quantitative retrievals and SDSU-Ash model simulations. The sensitivity of SSMIS brightness temperature measurements and ash total columnar content with respect to volcanic plume water vapor, ice content and surface background has been also investigated, showing a fairly good agreement between simulations and observations. The consistence in terms of estimation curve slopes is especially evident for SSMIS and MHS channels above 90 GHz.

The major conclusion of this Report D8.2 is the experimental confirm of the appealing potential of spaceborne microwave radiometer observations to monitor the erupted plume due to its sensitivity to the volcanic tephra in the proximity of the eruption vent (where satellite-based infrared measurements saturate their signature due to the presence of large particles and significant optical thickness). On the other hand, the major limitation of current spaceborne microwave radiometers for tephra loading detection and retrieval remains its poor spatial resolution (of the order of 15×15 km at frequency larger than 85 GHz) which limits the sensitivity to ash loadings larger than 0.1 kg/m^2 and coarse to large ash particles (larger than 50 microns of diameter).

Future developments should be devoted to the exploitation of dual-polarized weather radars, capable of measuring polarimetric observables both in amplitude and phase, for increasing the ash retrieval sensitivity and accuracy nearby the volcanic vent. Mixtures of hydrometeors and ash, undistinguishable from pure ash clouds using conventional radars, could be better investigated using dual-polarization instruments at higher frequencies. In this respect, weather radars at X-band might even show a better sensitivity with respect to the corresponding C-band systems having the same characteristics. The synergy among ground-based and satellite-based sensors should be further investigated as measurements from visible/infrared satellite imagers and ground-based lidars may be used as a complementary constraint for radar-based estimates due to their high sensitivity to fine ash particles.

REFERENCES

- Bonadonna, C., & Houghton, B. F. (2005). Total grain-size distribution and volume of tephra-fall deposits. *Bulletin of Volcanology*, 67 (10), 441-456.
- Delene, D. J., Rose, W. I. & Grody, N. C. (1996). Remote sensing of volcanic clouds using special sensor microwave imager data. *Journal of Geophysical Research*, 101 (B5), 11579-11588.
- Gangale, G., Prata, A. J., & Clarisse, L. (2010). The infrared spectral signature of volcanic ash determined from high-spectral resolution satellite measurements. *Remote Sensing of Environment*, 114 (2), 414-425.
- Gouhier, M., & Donnadieu, F. (2008). Mass estimations of ejecta from Strombolian explosions by inversion of Doppler radar measurements. *Journal of Geophysical Research*, 113 (B10202), 10202–10219.
- Grody, N. C., & Basist, A. N. (1996). Global identification of snowcover using SSM/I measurements. *IEEE Transactions on Geoscience and Remote Sensing*, 34 (1), 237-249.
- Grainger R. G., D. M. Peters, G. E. Thomas, A. J. A. Smith, R. Siddans, E. Carboni and A. Dudhia (2013), "Measuring volcanic plume and ash properties from space", Geological Society, London, Special Publications, 380, 1, 293-320, doi:10.1144/SP380.7.
- Harris, D. M., & Rose, Jr., W. I. (1983). Estimating particle sizes, concentrations, and total mass of ash in volcanic clouds using weather radar. *Journal of Geophysical Research*, 88 (C15), 10969-10983.
- Hort, M., Seyfried, R., & Vöge, M. (2003). Radar Doppler velocimetry of volcanic eruptions: theoretical considerations and quantitative documentation of changes in eruptive behaviour at Stromboli volcano, Italy. *Geophysical Journal International*, 154 (2), 515-532.
- Kitchen M. & P.M. Jackson (1993). Weather radar performance at long range. . Simulated and observed. *J. Appl. Meteor.*, 32, 975-985.
- Lacasse, C., Karlsdóttir, S., Larsen, G., Soosalu, H., Rose, W. I., & Ernst, G. G. J. (2004). Weather radar observations of the Hekla 2000 eruption cloud, Iceland. *Bulletin of Volcanology*, 66 (10), 457-473.
- Larsen, G., Guðmundsson, M. T., & Björnsson, H. (1998). Eight centuries of periodic volcanism at the center of the Iceland hotspot revealed by glacier tephrostratigraphy. *Geology*, 26 (10), 943-946.
- Marzano, F. S., Mugnai, A., Panegrossi, G., Pierdicca, N., Smith, E.A., & Turk, J. (1999). Bayesian estimation of precipitating cloud parameters from combined measurements of spaceborne microwave radiometer and radar. *IEEE Transactions on Geoscience and Remote Sensing*, 37 (1), 596-613.
- Marzano, F. S., Vulpiani, G., & Rose, W. I. (2006a). Microphysical characterization of microwave radar reflectivity due to volcanic ash clouds. *IEEE Transactions on Geoscience and Remote Sensing*, 44 (2), 313-327.
- Marzano, F. S., Barbieri, S., Vulpiani, G., & Rose, W. I. (2006b). Volcanic ash cloud retrieval by ground-based microwave weather radar. *IEEE Transactions on Geoscience and Remote Sensing*, 44 (11), 3235-3246.
- Marzano, F. S., Barbieri, S., Picciotti, E., & Karlsdóttir, S. (2010a). Monitoring sub-glacial volcanic eruption using C-band radar imagery. *IEEE Transactions on Geoscience and Remote Sensing*, 58 (1), 403-414.
- Marzano, F. S., Marchiotto, S., Textor, C., & Schneider, D. (2010b). Model-based Weather RADAR Remote Sensing of Explosive Volcanic Ash Eruption. *IEEE Transactions on Geoscience and Remote Sensing*, 48 (10), 3591-3607.
- Marzano, F. S., Lamantea, M., Montopoli, M., Di Fabio, S., & Picciotti, E. (2011). The Eyjafjöll explosive volcanic eruption from a microwave weather radar perspective. *Atmospheric Chemistry and Physics*, 11 (18), 9503-9518.
- Marzano, F. S., Picciotti, E., Vulpiani, G. & Montopoli, M. (2012a). Synthetic signatures of volcanic ash cloud particles from X-band dual-polarization radar. *IEEE Transactions on Geoscience and Remote Sensing*, 50 (1), 193-211.

- Marzano F.S., M. Lamantea, M. Montopoli, B. Oddsson & M.T. Gudmundsson, (2012b). Validating sub-glacial volcanic eruption using ground-based C-band radar imagery, *IEEE Transactions on Geoscience and Remote Sensing*, 50, DOI: 10.1109/TGRS.2011.2167017.
- Morton, R. R., Taylor, G., F.R.S, & Turner, J. S. (1956). Turbulent gravitational convection from maintained and instantaneous sources. *Proceedings of the Royal Society of London. Series A, Mathematical and Physical Sciences*, 234 (1196), 1-23.
- Oddsson, B., Guðmundsson, M.T., Larsen, G., & Karlsdóttir, S. (2008). Grímsvötn 2004: weather radar records and plume transport models applied to a phreatomagmatic basaltic eruption. IAVCEI 2008, Reykjavik (Iceland), August 18-24, 2008.
- Oddsson B., M.T. G., G. Larsen1, & S. Karlsdóttir (2012). Monitoring of the plume from the basaltic phreatomagmatic 2004 Grímsvötn eruption - application of weather radar and comparison with plume models. *Bull. of Volcanology*, 74 (6), 1395-1407.
- Prata, A. J., Barton, I. J., Johnson, R. W., Kamo, K., & Kingwell, J. (1991). Hazard from volcanic ash. *Nature*, 354 (25).
- Pulvirenti L., F.S. Marzano, and N. Pierdicca, (2007). Modeling microwave fully-polarimetric passive observations of a sea surface: a neural network approach. *IEEE Trans. Geosci. Rem. Sensing*, ISSN: 0196-2892, 45 (7), 2098-2117, 2007.
- Rodgers, C.D., *Inverse methods for atmospheric sounding. Theory and practice*, World Scientific Publishing, Singapore, 2000
- Rose, W. I., Kostinski, A.B., & Kelley, L. (1995). Real time C band radar observations of 1992 eruption clouds from Crater Peak, Mount Spurr Volcano, Alaska. *U.S. Geological Survey Bulletin*, 2139, 19-26.
- Sauvageot, H. (1992). *Radar meteorology*. Boston: Artech House Radar Library.
- Showstack, R. (2011). Iceland's Grímsvötn volcano erupts. *EOS, Transactions American Geophysical Union*, 92 (22), 187.
- Sparks, R.S.J., Bursik, M.I., Carey, S.N., Gilbert, J.S., Glaze, L., Sigurðsson, H., & Woods, A.W. (1997). *Volcanic plumes*. New York: John Wiley and Sons Ltd.
- Sparks, R. (1986). The dimensions and dynamics of volcanic eruption columns. *Bulletin of Volcanology*, 48 (1), 3-15.
- Spencer, R. W., Goodman, H. M., & Hood, R. E. (1989). Precipitation retrieval over land and ocean with the SSM/I - identification and characteristics of the scattering signal. *Journal of Atmosphere and Ocean Technology*, 6 (2), 254-273.
- Stewart, S.F., Pinkerton, H., Blackburn, G. A., & Guðmundsson, M.T. (2008). Monitoring active subglacial volcanoes: a case study using airborne remotely sensed imagery of Grímsvötn, Iceland. *International Journal of Remote Sensing*, 29 (22), 6501-6514.
- Stohl, A., Prata, A. J., Eckhardt, S., Clarisse, L., Durant, A., Henne, S., Kristiansen, N. I., Minikin, A., Schumann, U., Seibert, P., Stebel, K., Thomas, H. E., Thorsteinsson, T., Tørseth, K., & Weinzierl, B. (2011). Determination of time- and height-resolved volcanic ash emissions and their use for quantitative ash dispersion modeling: the 2010 Eyjafjallajökull eruption, *Atmospheric Chemistry and Physics*, 11 (9), 5541-5588.
- Thordarson, T., & Larsen, G., (2007). Volcanism in Iceland in historical time: volcano types, eruption styles and eruptive history. *Journal of Geodynamics*, 43 (1), 118-152.
- Tupper, A., Itikarai, I., Richards, M., Prata, F., Carn, S., & Rosenfeld, D. (2007). Facing the challenges of the international airways volcano watch: the 2004/05 eruptions of Manam, Papua New Guinea. *Weather and Forecasting*, 22 (1), 175-191.
- Vogfjörð, K., Jakobsdóttir, S., Guðmundsson, G. B., Roberts, M. J., Ágústsson, K., Arason, T., Geirsson, H., Karlsdóttir, S., Hjaltadóttir, S., Ólafsdóttir, U., Þorbjarnadóttir, B., Skaftadóttir, T., Sturkell, E., Jónasdóttir, E. B., Hafsteinsson, G., Sveinbjörnsson, H., Stefánsson, R., & Jónsson, T. (2005). Forecasting and monitoring a subglacial eruption in Iceland. *EOS, Transactions American Geophysical Union*, 86 (26), 245-252.
- Vulpiani G., Montopoli, M., Picciotti, E., & Marzano, F.S. (2011). On the use of a polarimetric X-band weather radar for volcanic ash clouds monitoring. *AMS Radar Conference*, Pittsburgh (PA - USA), September 26-30, 2011.
- Wen S., & Rose, W. I. (1994). Retrieval of sizes and total masses of particles in volcanic clouds using AVHRR bands 4 and 5. *Journal of Geophysical Research*, 99 (D3), 5421-5431.
- Wilheit, T., Adler, R., Avery, S., Barrett, E., Bauer, P., Berg, W., Chang, A., Ferriday, J., Grody, N., Goodman, S., Kidd, C., Kniveton, D., Kummerow, C., Mugnai, A., Olson, W., Petty, G., Shibata, A., & Smith, E.A. (1994). Algorithms for the retrieval of rainfall from passive microwave measurements. *Remote Sensing Reviews*, 11 (1-4), 163-194.
- Wilson, L. (1972). Explosive volcanic eruptions-II: the atmospheric trajectories of pyroclasts. *Geophysical Journal of the Royal Astronomical Society*, 30 (2), 381-392.

-
- Wilson, L., Sparks, R. S. J., Huang, T. C., & Watkins, N. D. (1978). The control of volcanic column heights by eruption energetics and dynamics. *Journal of Geophysical Research*, 83 (B4), 1829-1836.
- Yan, B., & Weng, F. (2008). Intercalibration between special sensor microwave imager/sounder and special sensor microwave imager. *IEEE Transactions on Geoscience and Remote Sensing*, 46 (9), 984-995.
- Yu, T., Rose, W. I., & Prata, A. J. (2002). Atmospheric correction for satellite based volcanic ash mapping and retrievals using “split-window” IR data from GOES and AVHRR. *Journal of Geophysical Research*, 107 (D16), 4311-4330.
- Zrnic D.S. & A. Ryzkov (1996). Advantages of rain measurements using specific differential phase. *J. Atm. Ocean. Tech.*, 13, 454-464.
- Zehner C., Ed. (2010). Monitoring Volcanic Ash from Space. Proceedings of the ESA-EUMETSAT workshop on the 14 April to 23 May 2010 eruption at the Eyjafjoll volcano, South Iceland. Frascati, Italy, 26-27 May 2010. ESA-Publication STM-280. doi:10.5270/atmch-10-01.